Available online at www.sciencedirect.com

ScienceDirect

Journal of Sound and Vibration 313 (2008) 449–471

JOURNAL OF SOUND AND VIBRATION

www.elsevier.com/locate/jsvi

Numerical simulation of a slit resonator in a grazing flow under acoustic excitation

Christopher K.W. Tam[a,*], Hongbin Ju[a], Bruce E. Walker[b]

[a]*Department of Mathematics, Florida State University, Tallahassee, FL 32306-4510, USA*
[b]*Channel Islands Acoustics, 676 West Highland Drive, Camarillo, CA 93010, USA*

Received 1 February 2006; received in revised form 20 November 2007; accepted 3 December 2007
Handling Editor: P. Davies
Available online 4 February 2008

Abstract

It is known experimentally that a grazing flow has significant influence on the performance of a resonant acoustic liner. As yet, detailed understanding of the effect in fluid dynamics or acoustics terms is not available. One principal reason for this is the small size of the openings of the resonators of present day jet engine acoustic liners. The small size of the holes makes in-depth experimental observation and mapping of the fluid flow field around the opening of a resonator in the presence of a grazing flow extremely difficult. As a result, there is a genuine lack of data leading directly to a lack of understanding. The face sheet of an acoustic liner is entirely covered with holes (the openings of resonators underneath). There is, therefore, a possibility of fluid mechanical interaction between neighboring resonators. However, evidence for such interaction is not available at this time. One of the objectives of the present work is to shed light on whether this is possible and what is a possible interaction mechanism. In this study, numerical simulations of the flow field around a slit resonator in the presence of a grazing flow under acoustic forcing are carried out. It is observed that at high sound pressure level, vortices are shed from the corners of the resonator opening. Some of these vortices merge together. Others are absorbed by the wall boundary layer or dissipated by viscosity. The simulated results indicate that a strong merged vortex is convected downstream by the grazing flow and persists for a long distance. This suggests that possible fluid mechanical interaction between neighboring resonators of an acoustic liner could, indeed, be possible because of the interference of this convected vortex with the flow field of the downstream resonator. This interaction, as far as is known, has not been included in any theoretical or semi-empirical model of acoustic liners. Detailed formulation of the computational model, as well as computational algorithm, is provided. The computation code is verified by comparing computed results with an exact linear solution and also validated by comparing with measurements of a companion experiment.

---

1. Introduction

An acoustic liner is, without doubt, one of the most effective means for suppressing jet engine fan noise. The study of the performance of acoustic liners and their damping mechanisms began in earnest with the introduction of commercial jet aircraft. A few of the influential early works are Ingard and Labate [1], Ingard

---

[*] Corresponding author.
E-mail address: tam@math.fsu.edu (C.K.W. Tam).

doi:10.1016/j.jsv.2007.12.018

and Ising [2], Melling [3] and Zinn [4]. From that time on, there have been numerous investigations on this subject. Many investigations were experimental. Others involved the development of semi-empirical or theoretical models. More recently, there were also studies by direct numerical simulation. It soon became clear that grazing flow inside a jet engine had a significant impact on acoustic liner performance. As a result, a considerable body of research work was devoted to the effect of grazing flow (Refs. [5–11]).

Aircraft noise is a sensitive environmental issue as well as a critical factor in aircraft certification. The introduction of newer high-by-past ratio engines has significantly lowered the level of jet noise. Thus the need to reduce fan noise becomes more urgent. This, in turn, leads to vigorous new research activities on grazing flow effects on acoustic liner performance. In the past, several approaches had been followed aiming to predict the impedance of liners in the presence of flow. Semi-empirical models of flow effects were developed by Rice [12], Hersh et al. [13], Dupère and Dowling [14], Elnady and Boden [15], just to name a few. The use of a vortex sheet/thin shear layer model led to sophisticated mathematical analysis by Ronneberger [16], Howe et al. [17], Kaji et al. [18], Grace et al. [19], Howe [20], and Jing et al. [21]. However, Jing et al. pointed out that some of the vortex sheet models had not been verified experimentally. The resistance and reactance of an acoustic liner in the presence of a grazing flow are determined by complex fluid structure interaction. To deal with such complexities, a number of investigators, e.g., Kooi and Sarin [9], Nelson et al. [22], Worraker and Halliwell [23], Malmary and Carbonne [24], Walker and Hersh [25], chose to take an experimental approach. However, because the openings of the resonators of an acoustic liner are very small, there is a lack of detailed experimental measurements of the micro-fluid flow field around the mouths of the resonators. This is so, even though there has been considerable agreement that most acoustic dissipation takes place in these regions. At the present time, although good progress has been made in describing and quantifying the gross properties of acoustic liners (e.g., the works of Watson et al. [26,27]), there is still a lack of basic understanding of the dissipative mechanisms associated with micro-scale fluid flow field around an individual resonator in the presence of a grazing flow.

It is useful to point out that flow-induced tones are very likely to occur for a cavity with an opening large compared with the thickness of the shear layer spanning over it (see, for example, the works of Colonius [28], Gloerfelt et al. [29] and Larcheveque et al. [30]). For a comprehensive review of such flow-induced tones, referred to as cavity tones, one may consult the recent work by Takeda and Shieh [31]. Cavity tones are generated by a feedback loop driven by the instability waves of the shear layer.

There are two types of cavity tones (see Ref. [32]). For shallow cavities, the feedback is accomplished by sound waves generated by the interaction of shear layer instability waves and the trailing edge of the cavity. The sound waves generated propagate upstream inside the cavity until they reach the upstream wall. Upon impinging on the cavity wall, the scattered waves excite the shear layer, resulting in the generation of new instability waves. The instability waves are amplified as they propagate downstream along the shear layer. On reaching the downstream wall of the cavity, the instability waves interact with the trailing edge and produce new sound waves. In this way, the feedback loop is completed. This type of cavity tones is generally referred to as Rossiter [33] tones. For deep cavity, the feedback is accomplished by the excitation of the acoustic depth modes of the cavity. The coupling of an acoustic depth mode and the shear layer instability waves is responsible for the emission of tones. Cavity tones, however, do not occur for acoustic liner cavities (resonators). The reason is that the openings of these resonators are small compared to the thickness of the boundary layer flowing over the surface of the liner. A useful rule of thumb is that shear layer instability waves have wave lengths which are approximately six times the thickness of the shear layer. Thus, unless the resonator opening is about six times the boundary layer thickness or larger, there will not be any shear layer instability and hence no cavity tones.

With rapid advances in computational aeroacoustics methodology and the availability of fast parallel computers, it becomes possible to investigate the flow physics of acoustic liners by numerical simulation. Unlike experimental approach, the small size of resonator openings of an acoustic liner presents no difficulty to numerical simulation. In an earlier work, Tam and Kurbatskii [34] found that the flow around the mouth of a resonator of an acoustic liner could take on two distinct regimes. At low incident sound pressure level, acoustic dissipation was accomplished by the development of strong oscillatory shear layers adjacent to the walls at the opening of a resonator. Acoustic energy was dissipated by viscous friction in the oscillatory shear layers. At high level of incident sound, the flow was dominated by vortex shedding from the corners of the resonator opening. The kinetic energy associated with the rotation of the shed vortices was subsequently dissipated by molecular viscosity. The transfer of acoustic energy to the rotational kinetic energy of the shed vortices and then dissipation by viscosity is the dominant dissipation mechanism. This acoustic wave dissipation mechanism by vortex shedding was confirmed directly in the work of Tam et al. [35]. In their work, experimental measurements of the absorption coefficients of a resonator were found to agree well with numerical simulation results. The numerical simulation results were determined by direct measurement of the kinetic energy transferred to the shed vortices.

In a collaborative work between NASA Langley Research Center and the Florida State University, a detailed study of the impedance and flow field around slit resonators in a normal impedance tube was carried out experimentally and by numerical simulation [36]. Good agreements were obtained between experimental and simulation results in all cases considered. Of special interest is that, in this study, broadband sound waves were used as an input in addition to discrete frequency sound. It was observed that under broadband sound excitation, vortex shedding, although more random and chaotic, was still the dominant dissipation mechanism. Further, to enhance vortex shedding, beveled slits were also used to form the openings of slit resonators. It was observed that there was, indeed, stronger vortex shedding and larger absorption coefficient.

The purpose of the present investigation is to examine the effect of grazing flow on the performance of slit resonators by direct numerical simulation. Previously, Tam and Kurbatskii [37] had computed the flow field associated with grazing flow over a slit resonator in an open domain. The present work may, therefore, be regarded as an extension of this work. Here emphasis is on determining whether there could be fluid mechanical interaction between neighboring resonators of an acoustic liner due to the convection effect of grazing flow. All previous semi-empirical, as well as theoretical, models of acoustic liners do not account for such possible interaction. In addition, a companion experiment was performed. The experimental results are used to validate the present numerical simulation code. It will be confirmed that the earlier conclusion of Tam and Kurbatskii [34] that, depending on the sound pressure level, the acoustic damping mechanism changes from viscous dissipation in the oscillatory shear layer to chaotic vortex shedding remains valid even in the presence of a Mach 0.2 grazing flow.

The remainder of this paper is as follows. In Section 2, the computation model is presented. Verification of the computation algorithm and computer code by comparing numerical solution with exact (linear) analytical solution is discussed in Section 3. The main results of this work are reported in Section 4. They consist of steady-state flow pattern inside a resonator, vortex shedding at high incident sound pressure level, and comparison between flow field streamline patterns calculated from numerical simulation data and direct experimental measurements at low sound pressure levels. A summary and conclusions are provided at the end of this paper.

2. Computational model

The companion experiment of the present numerical simulation effort uses a wind tunnel, which is 24 in (61 cm) wide and 10 in (25.4 cm) high as shown in Fig. 1. It is 5 in (12.7 cm) deep in the third dimension.

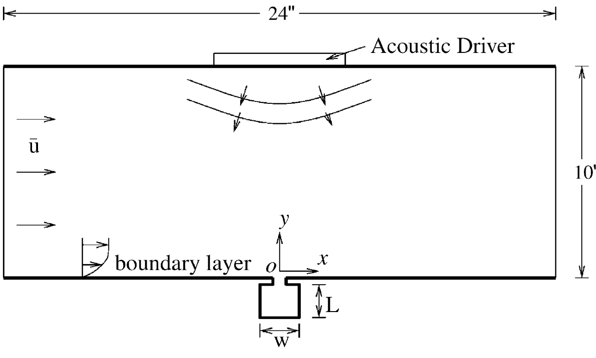

Fig. 1. Flow configuration and computation domain.

A two-dimensional resonator with a dimension of $W = 2$ in (5.08 cm) and $L = 2.262$ in (5.745 cm) is housed at the bottom of the wind tunnel. The resonator has an opening of 0.25 in (0.635 cm) width and 0.125 in (0.3175 cm) thickness, which spans the full 5 in depth of the test section. These dimensions were chosen to provide a Helmholtz resonance frequency of 625 Hz. An acoustic driver is mounted on the top of the wind tunnel. To begin an experiment or simulation, the acoustic driver is turned on. The acoustic waves generated create an incident sound field impinging on the resonator. In the numerical simulation, the geometry and dimensions of the experimental facility are used. The wind tunnel produces a nearly uniform flow except adjacent to a wall. On the bottom wall, a boundary layer is formed. This is the grazing flow condition outside the resonator.

2.1. Mesh design

In addition to an accurate time-marching scheme, a well-designed mesh is necessary to ensure a high-quality numerical simulation. The present grazing flow problem involves some very large disparate length scales. The smallest scale is the viscous scale associated with the Stokes layer. In the presence of an oscillating pressure field, a Stokes layer is formed adjacent to a wall. Stokes layer consists of sheets of fluid oscillating parallel to the wall with a wavelength λ given by (see Ref. [38])

$$\lambda_{\text{Stokes}} = \left(\frac{4\pi v}{f}\right)^{1/2},$$

where v is the kinematic viscosity of the fluid and f is the frequency of oscillation. In this work, the 7-point stencil dispersion-relation-preserving scheme [39] is used for all time marching computations. This scheme is designed to offer good accuracy if 7–8 mesh points per wavelength are used in the computation. Thus, the spatial mesh spacing requirement for the resolution of the Stokes layer is

$$\Delta x_{\text{Stokes}} = \frac{1}{8}\left(\frac{4\pi v}{f}\right)^{1/2}. \tag{1}$$

To be able to provide adequate resolution in different parts of the physical domain, a multi-size mesh is used in the numerical simulation. The smallest size mesh is placed at the mouth of the resonator as shown in Fig. 2.

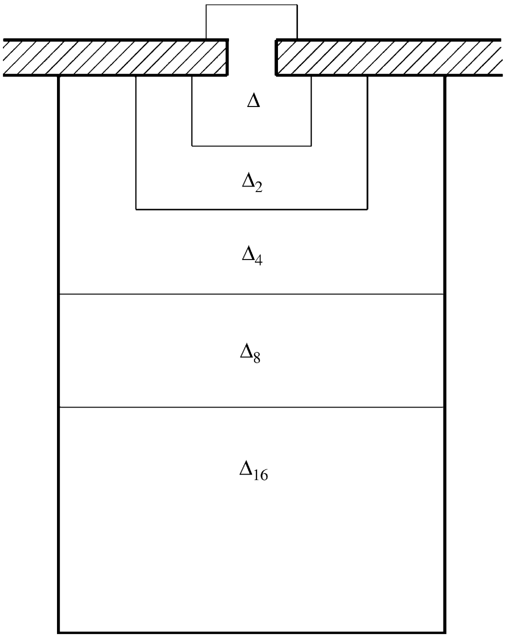

Fig. 2. Mesh design inside the resonator.

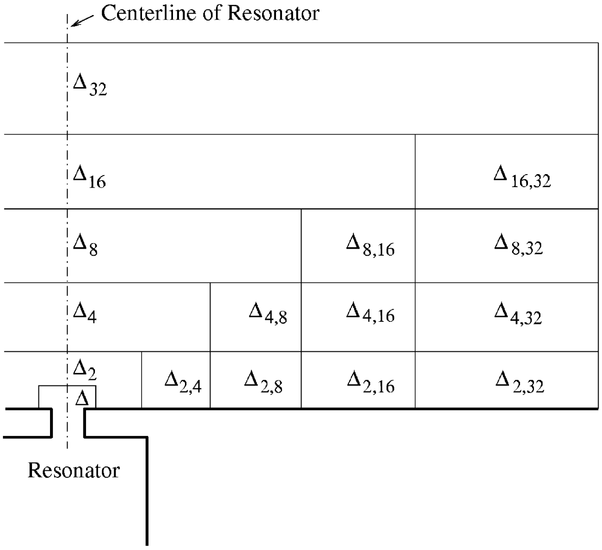

Fig. 3. Mesh design in the wind tunnel.

The mesh size is determined by formula (1), with $\nu = 0.0225\,\mathrm{in}^2/\mathrm{s}$ ($0.145\,\mathrm{cm}^2/\mathrm{s}$) (kinematic viscosity for air) and an incident sound frequency of 625 Hz. It is found $\Delta x_{\mathrm{Stokes}} = 0.002657$ in (0.00675 cm). The resonator opening has a width of 0.25 in (0.635 cm) and a depth of 0.125 in (0.3175 cm). Therefore, by using a square meshes in an array of 120×60 gives a mesh size $\Delta = 0.00208$ in (0.00528 cm). This meets the requirement of providing sufficient resolution for the Stokes layers adjacent to the wall. The notations Δ_2, Δ_4, Δ_8, Δ_{16} and Δ_{32} will be used to denote square meshes of size equal to 2, 4, 8, 16 and 32 times that of Δ. Fig. 2 shows the mesh design used inside the resonator. The mesh size increases by a factor of 2 as one goes into the next mesh block starting from the mouth of the resonator.

Fig. 3 shows the mesh design inside the wind tunnel. Only half the computation domain is shown. The other half is symmetric about the centerline of the resonator and acoustic driver. Away from the mouth of the resonator in the upstream and downstream directions, rectangular meshes are used. The notation $\Delta_{2n,2m}$ denotes a rectangular mesh with mesh size $2n\Delta$ in the vertical direction and $2m\Delta$ in the horizontal direction. The largest size mesh used is Δ_{32} in the uppermost mesh layer adjacent to the top wall. With the mesh arrangement decided, it is easy to check that the mesh size change across a boundary of any subdomain is 2.

2.2. Governing equations

Non-dimensional variables are used. The following scales are adopted:

$$\text{Length scale} = \text{width of slit} = 0.25\,\text{in}\ (0.635\,\text{cm}),$$

$$\text{Velocity scale} = a_0\ (\text{speed of sound}),$$

$$\text{Time scale} = \frac{\text{width of slit}}{a_0},$$

$$\text{Density scale} = \rho_0\ (\text{density of incoming flow}),$$

$$\text{Pressure and stresses scale} = \rho_0 a_0^2.$$

The compressible Navier–Stokes equations are

$$\frac{\partial \rho}{\partial t} + u\frac{\partial \rho}{\partial x} + v\frac{\partial \rho}{\partial y} + \rho\left(\frac{\partial u}{\partial x} + \frac{\partial v}{\partial y}\right) = 0, \tag{2}$$

$$\frac{\partial u}{\partial t}+u\frac{\partial u}{\partial x}+v\frac{\partial u}{\partial y}=-\frac{1}{\rho}\frac{\partial p}{\partial x}+\frac{1}{\rho}\left(\frac{\partial \tau_{xx}}{\partial x}+\frac{\partial \tau_{xy}}{\partial y}\right), \tag{3}$$

$$\frac{\partial v}{\partial t}+u\frac{\partial v}{\partial x}+v\frac{\partial v}{\partial y}=-\frac{1}{\rho}\frac{\partial p}{\partial y}+\frac{1}{\rho}\left(\frac{\partial \tau_{xy}}{\partial x}+\frac{\partial \tau_{yy}}{\partial y}\right), \tag{4}$$

$$\frac{\partial p}{\partial t}+u\frac{\partial p}{\partial x}+v\frac{\partial p}{\partial y}+\gamma p\left(\frac{\partial u}{\partial x}+\frac{\partial v}{\partial y}\right)=0, \tag{5}$$

$$\tau_{xx}=\frac{2}{Re}\frac{\partial u}{\partial x},\quad \tau_{xy}=\tau_{yx}=\frac{1}{Re}\left(\frac{\partial u}{\partial y}+\frac{\partial v}{\partial x}\right),\quad \tau_{yy}=\frac{2}{Re}\frac{\partial v}{\partial y}, \tag{6}$$

where $Re = Ta_0/\nu$ is the Reynolds number based on T (width of slit) and a_0. Viscous dissipation is neglected in the energy equation. In the numerical computation, the full viscous equations are used only in regions with mesh size Δ and 2Δ. These are regions close to the bottom wall of the wind tunnel and the mouth of the resonator. Outside these regions, the viscous terms are dropped (Euler equations are used) as the flow is nearly inviscid.

The governing equations are solved computationally using the multi-size-mesh multi-time-step dispersion-relation-preserving scheme [40]. This is a variation of the original dispersion-relation-preserving scheme of Tam and Webb [39]. To ensure numerical accuracy, a minimum of 7 mesh points per wavelength throughout the entire computation domain is used. The time marching solution begins with zero acoustic disturbances inside the wind tunnel with the resonator blocked off. The solution with the given inflow is marched to a time steady state. At this time, the acoustic driver is turned on and the resonator is unblocked. The numerical solution is then marched in time until a time periodic state is attained.

2.3. Numerical boundary conditions

In the experiment, an acoustic driver is housed on the top wall of the wind tunnel. This acoustic driver sends sound waves into the wind tunnel. The sound waves propagate across the wind tunnel, impinging on the bottom wall and the resonator. Part of the sound waves is reflected back. On reaching the acoustic driver or the wall on the top, the reflected sound waves are once more reflected. Because of the repeated reflection, a standing wave pattern eventually develops inside the wind tunnel. Since acoustic energy is pumped into the wind tunnel by the acoustic driver, in order to establish a time periodic state, sound energy has to be leaked out from the two open boundaries of the computation domain. This observation is taken into consideration in the choice of upstream and downstream boundary conditions. A quality numerical treatment of the wind tunnel boundaries is crucial to the accuracy of the simulation. This includes the prescription of numerical boundary condition on the top and bottom wall of the wind tunnel as well as the open ends on the two sides as shown in Fig. 1.

The no-slip boundary conditions, $u = 0$, $v = 0$, are used at the bottom wall and around the opening of the resonator. On the top wall, the motion of the acoustic driver is modeled by the following boundary condition:

$$y=H,\quad v=Re\begin{cases} -A\,\mathrm{e}^{-(\ln 2)((x+(L/2))/b)^2-\mathrm{i}\omega t}, & x<-\dfrac{L}{2},\\ -A\,\mathrm{e}^{-\mathrm{i}\omega t}, & -\dfrac{L}{2}\leqslant x\leqslant \dfrac{L}{2},\\ -A\,\mathrm{e}^{-(\ln 2)((x-(L/2))/b)^2-\mathrm{i}\omega t}, & \dfrac{L}{2}<x, \end{cases} \tag{7}$$

where L is the size of the acoustic driver and b is a short transition width. In the numerical simulation, the wall boundary conditions are enforced by the Ghost Point method. Two ghost values, namely, p and τ (the shear stress), are used for imposing the no-slip boundary conditions. For the top wall, only one ghost value of p is needed to enforce boundary condition Eq. (7).

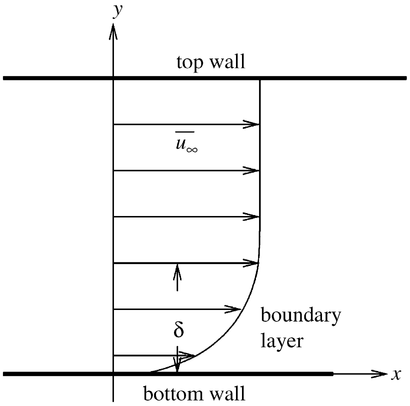

Fig. 4. Mean flow velocity profile used by numerical simulation at the inflow boundary.

2.4. Inflow boundary conditions

At the inflow boundary, the incoming mean flow is specified. The boundary layer on the top wall is ignored (see Fig. 4). The boundary layer adjacent to the bottom wall is important as it interacts with the slit resonator. The boundary layer is assumed to have a Blasius profile, i.e., at $x = x_L$ (the location of the left boundary of the computation domain),

$$\bar{u}(y) = \begin{cases} \bar{u}_\infty, & y > \delta, \\ \bar{u}_{\text{Blasius}}(y), & y \leqslant \delta. \end{cases} \tag{8}$$

The boundary layer thickness δ or the displacement thickness δ^* is assigned the same value as that of the companion experiment ($\delta = 0.25\,\text{in}$). Blasius profile is expressed in terms of similarity variable $\eta = 5y/\delta$:

$$\frac{\bar{u}_{\text{Blasius}}(y)}{u_\infty} = f'(\eta).$$

$f(\eta)$ is tabulated in many books, e.g. Ref. [38].

Now, at the inflow boundary, there are outgoing acoustic disturbances. To prevent them from reflecting back into the computation domain, a perfectly matched layer absorbing boundary condition is used. Let

$$\begin{bmatrix} \rho \\ u \\ v \\ p \end{bmatrix} = \begin{bmatrix} 1 \\ \bar{u}(y) \\ 0 \\ 1/\gamma \end{bmatrix} + \begin{bmatrix} \rho' \\ u' \\ v' \\ p' \end{bmatrix}, \tag{9}$$

where the first column vector on the right is the mean flow and the second represents outgoing disturbances. Since there is flow normal to the perfectly matched layer, the split variable perfectly matched layer method is unstable. In this work, the most recent perfectly matched layer boundary method proposed by Hu [41] is employed. According to the formulation, the perfectly matched layer equation is

$$\frac{\partial \mathbf{u}}{\partial t} + \mathbf{A}\frac{\partial \mathbf{u}}{\partial x} + \mathbf{B}\frac{\partial}{\partial y}(\mathbf{u} + \sigma_x \mathbf{q}) + \sigma_x \mathbf{u} + \frac{\sigma_x M}{1 - M^2}\mathbf{A}\mathbf{u} = 0, \tag{10}$$

where M is the flow Mach number and

$$\mathbf{u} = \begin{bmatrix} \rho' \\ u' \\ v' \\ p' \end{bmatrix}, \quad \mathbf{A} = \begin{bmatrix} M & 1 & 0 & 0 \\ 0 & M & 0 & 1 \\ 0 & 0 & M & 0 \\ 0 & 1 & 0 & M \end{bmatrix}, \quad \mathbf{B} = \begin{bmatrix} 0 & 0 & 1 & 0 \\ 0 & 0 & 0 & 0 \\ 0 & 0 & 0 & 1 \\ 0 & 0 & 1 & 0 \end{bmatrix}.$$

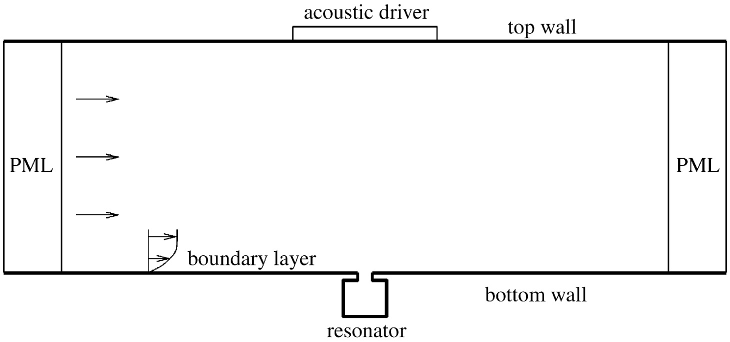

Fig. 5. Perfectly matched layers at the inflow and outflow boundaries of the computation domain.

σ_x is the damping coefficient of the perfectly matched layer and

$$\frac{\partial \mathbf{q}}{\partial t} = \mathbf{u}. \tag{11}$$

In the boundary layer, M is replaced by $\bar{u}(y)$. Fig. 5 shows the perfectly matched layer at the inflow and outflow boundaries of the computation domain.

2.5. *Outflow boundary conditions*

The outflow boundary condition is treated in a similar way as at the inflow boundary. The first task is to determine the mean flow profile.

It will again be assumed that the boundary layer at the outflow boundary has a Blasius profile. The length of the computation domain is 24.33 in, so that there is little change in the boundary layer thickness from the inflow to the outflow. Similar to the numerical treatment at the inflow boundary (exactly as in Eq. (9)), let

$$\begin{bmatrix} \rho \\ u \\ v \\ p \end{bmatrix} = \begin{bmatrix} 1 \\ \bar{u}(y) \\ 0 \\ 1/\gamma \end{bmatrix} + \begin{bmatrix} \rho' \\ u' \\ v' \\ p' \end{bmatrix}.$$

The unknown vector (second vector on the right side) is governed by an equation similar to Eq. (10). The computation can also be carried out in the same way.

3. Verification of numerical algorithm and computer code

When the acoustic driver is operating at low power, the acoustic wave amplitude inside the wind tunnel is small. Under this circumstance, the problem is effectively linear. It turns out that an exact analytical solution of the linear problem without the resonator can be found. This analytical solution is used here to verify the numerical algorithm and computer code.

3.1. *Analytical solution*

The linear problem is as shown in Fig. 6. The governing equations are the linearized Euler equations. In dimensionless form, they are (for clarity, a ˆ denotes a variable of the linear problem)

$$\frac{\partial \hat{\rho}}{\partial t} + M\frac{\partial \hat{\rho}}{\partial x} + \left(\frac{\partial \hat{u}}{\partial x} + \frac{\partial \hat{v}}{\partial y}\right) = 0, \tag{12}$$

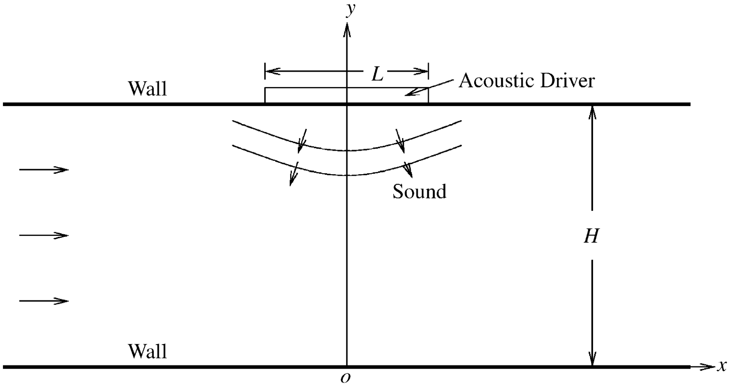

Fig. 6. Configuration of wind tunnel for the linear problem.

$$\frac{\partial \hat{u}}{\partial t} + M\frac{\partial \hat{u}}{\partial x} = -\frac{\partial \hat{p}}{\partial x}, \tag{13}$$

$$\frac{\partial \hat{v}}{\partial t} + M\frac{\partial \hat{v}}{\partial x} = -\frac{\partial \hat{p}}{\partial y}, \tag{14}$$

$$\frac{\partial \hat{p}}{\partial t} + M\frac{\partial \hat{p}}{\partial x} + \left(\frac{\partial \hat{u}}{\partial x} + \frac{\partial \hat{v}}{\partial y}\right) = 0. \tag{15}$$

The boundary conditions are

$$y = 0, \quad \hat{v} = 0, \tag{16}$$

$$y = H, \quad \hat{v} = Re\begin{cases} -A\,\mathrm{e}^{-(\ln 2)((x+(L/2))/b)^2 - \mathrm{i}\omega t}, & x < -\dfrac{L}{2}, \\ -A\,\mathrm{e}^{-\mathrm{i}\omega t}, & -\dfrac{L}{2} \leqslant x \leqslant \dfrac{L}{2}, \\ -A\,\mathrm{e}^{-(\ln 2)((x-(L/2))/b)^2 - \mathrm{i}\omega t}, & \dfrac{L}{2} < x. \end{cases} \tag{17}$$

As $x \to \pm\infty$, the solution represents outgoing waves. Boundary condition Eq. (17) is the same as that used in the numerical simulation.

To solve the above problem, the first step is to factor out the time dependence $\mathrm{e}^{-\mathrm{i}\omega t}$. Let

$$\begin{bmatrix} \hat{u} \\ \hat{v} \\ \hat{p} \end{bmatrix} = Re\left\{ \begin{bmatrix} \tilde{u}(x,y) \\ \tilde{v}(x,y) \\ \tilde{p}(x,y) \end{bmatrix} \mathrm{e}^{-\mathrm{i}\omega t} \right\}. \tag{18}$$

The governing equations for $\tilde{u}$, $\tilde{v}$ and $\tilde{p}$ can easily be found by substituting Eq. (18) into Eqs. (13)–(15). The corresponding boundary conditions are found by substituting Eq. (18) into Eqs. (16) and (17). The resulting problem has constant coefficients. The x-dependence may now be reduced to algebraic dependence by the application of Fourier transform. The Fourier transform and its inverse are defined by

$$\bar{u}(y,k) = \frac{1}{2\pi}\int_{-\infty}^{\infty} \tilde{u}(x,y)\,\mathrm{e}^{-\mathrm{i}kx}\,\mathrm{d}x, \quad \tilde{u}(x,y) = \int_{-\infty}^{\infty} \bar{u}(y,k)\,\mathrm{e}^{\mathrm{i}kx}\,\mathrm{d}k, \tag{19}$$

where k is the Fourier transform variable.

The transformed problem (denoted by an overbar) is

$$-\mathrm{i}(\omega - Mk)\bar{u} = -\mathrm{i}k\bar{p}, \tag{20a}$$

$$-\mathrm{i}(\omega - Mk)\bar{v} = -\frac{\mathrm{d}\bar{p}}{\mathrm{d}y}, \tag{20b}$$

$$-\mathrm{i}(\omega - Mk)\bar{p} + \mathrm{i}k\bar{u} + \frac{\mathrm{d}\bar{v}}{\mathrm{d}y} = 0. \tag{20c}$$

By eliminating $\bar{u}$ and $\bar{p}$, an equation for $\bar{v}$ is found:

$$\frac{\mathrm{d}^2\bar{v}}{\mathrm{d}y^2} - (1-M^2)\left(k + \frac{\omega}{1-M}\right)\left(k - \frac{\omega}{1+M}\right)\bar{v} = 0.$$

The solution for $\bar{v}$ and its companion variable $\bar{p}$ is

$$\bar{v}(y,k) = B\left[\mathrm{e}^{(1-M^2)^{1/2}(k+(\omega/(1-M)))^{1/2}(k-(\omega/(1+M)))^{1/2}y} - \mathrm{e}^{-(1-M^2)^{1/2}(k+(\omega/(1-M)))^{1/2}(k-(\omega/(1+M)))^{1/2}y}\right], \tag{21}$$

$$\bar{p}(y,k) = \frac{\mathrm{i}(\omega - Mk)}{(1-M^2)(k+\omega/(1-M))(k-\omega/(1+M))}\,\frac{\mathrm{d}\bar{v}(y,k)}{\mathrm{d}y}. \tag{22}$$

The unknown coefficient B is determined by the Fourier transform of boundary condition Eq. (17). It is easy to verify that the Fourier transform of $\hat{v}$ at $y = H$ is

$$\bar{v}(H,k) = \frac{1}{2\pi}\int_{-\infty}^{\infty}\hat{v}(x,H)\,\mathrm{e}^{-\mathrm{i}kx}\,\mathrm{d}x = -\frac{A}{2\pi}\left\{\left(\frac{\pi}{\ln 2}\right)^{1/2} b\,\mathrm{e}^{-k^2b^2/4\ln 2}\right. \\ \left.\times Re\left\{\left[\left(1-\mathrm{erf}\left(-\frac{\mathrm{i}kb}{2(\ln 2)^{1/2}}\right)\right)\mathrm{e}^{\mathrm{i}kL/2}\right] + \frac{2\sin(k(L/2))}{k}\right\}\right\}, \tag{23}$$

where erf( ) is the error function. On combining Eqs. (21) and (23), B is found to be

$$B = \frac{\bar{v}(H,k)}{2\sinh[(1-M^2)^{1/2}(k+\omega/(1-M))^{1/2}(k-\omega/(1+M))^{1/2}H]}. \tag{24}$$

At this stage, the complete solution in Fourier space is known. On inverting the Fourier transform, the pressure distribution inside the wind tunnel may be calculated:

$$p(x,y,t) = Re\left\{\int_{-\infty}^{\infty}\bar{p}(y,k)\,\mathrm{e}^{\mathrm{i}kx-\mathrm{i}\omega t}\,\mathrm{d}k\right\}. \tag{25}$$

The k-integral of Eq. (25) may be evaluated by numerical integration along the slightly deformed contour as shown in Fig. 7. The branch cuts of the square root functions are also shown in this figure. The evaluation of the integral is carried out numerically.

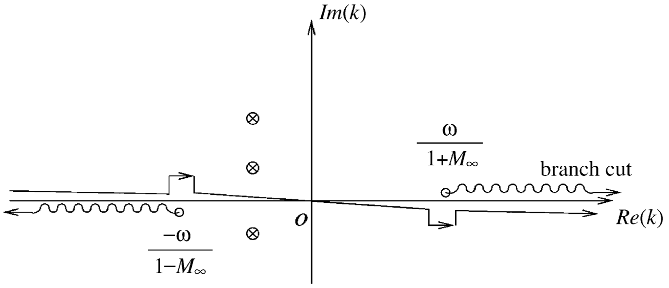

Fig. 7. The inversion contour in the k-plane. Shown also are branch cuts (o∿∿∿→) and poles (⊗) of the integrand.

3.2. Comparisons between numerical and analytical solutions

Comparisons will now be made between the results of the numerical solution and the analytical solution. The pressure contour distribution inside the wind tunnel when the acoustic driver is operating at 625 Hz will be compared first. The wind tunnel has a Mach number of 0.15. In the numerical simulation the full Navier–Stokes equations are solved. Because of molecular viscosity, a thin boundary layer associated with the mean flow develops over the bottom wall. The boundary layer thickness at the inflow is 0.25 in (0.635 cm). The analytic model is inviscid without a boundary layer. However, it must be pointed out that at 625 Hz the acoustic wavelength is over 21 in (53.34 cm). This is much longer than the height of the wind tunnel (10 in or 25.4 cm) and is equal to many times the boundary layer thickness. Since the acoustic scale is long, the velocity gradient associated with the sound waves is small. Hence viscous effect is not expected to be important. Fig. 8 shows two sets of pressure contours. One set is found through numerical simulation. The other set is from the analytic solution. As can be seen, there is good agreement over the entire computation domain. The good agreement provides a useful verification of the computer code.

Another useful test of the accuracy of the computer code is to make use of the transient solution. When the acoustic driver is first turned on, many acoustic duct modes of the wind tunnel are excited. These duct modes, over time, exit the computation domain through the two open ends of the numerical wind tunnel. They are then absorbed by the perfectly matched layers. However, there are duct modes with zero group velocity. These waves do not propagate and are the last transient component to vanish from the computation domain. If the frequency of the zero group velocity duct mode differs slightly from the forcing frequency, then the pressure time history at any point inside the wind tunnel will exhibit amplitude modulation. Fig. 9 shows the pressure time history at a point 2.25 in (5.715 cm) downstream from the center of the acoustic driver on the bottom wall of the wind tunnel. For convenience, the oscillation period of the acoustic driver is used as time unit. The phenomenon of amplitude modulation can clearly be seen in this figure.

The frequency of the duct mode with zero group velocity can be calculated from the dispersion relation. The dispersion relation of all the duct modes are given by the zeros of denominator of $\bar{p}$ or that of Eq. (24) in the k-plane. Since the zeros of $\sinh(z)$ are located at $z = \mathrm{i}n\pi$ $(n = 0, \pm 1, \pm 2, \ldots)$, it follows that the dispersion relations are

$$k^2 + \frac{2M}{1 - M^2}\,\omega k - \frac{\omega^2}{1 - M^2} + \frac{n^2\pi^2}{(1 - M^2)H^2} = 0. \tag{26}$$

By differentiating Eq. (26) with respect to k, the group velocity can easily be found to be

$$\frac{\mathrm{d}\omega}{\mathrm{d}k} = \frac{k + (M\omega/(1 - M^2))}{(\omega - Mk)/(1 - M^2)}. \tag{27}$$

Thus, the wavenumber k_0 and angular frequency ω_0 of the zero group velocity duct mode are related by

$$k_0 = -\frac{M}{1 - M^2}\,\omega_0. \tag{28}$$

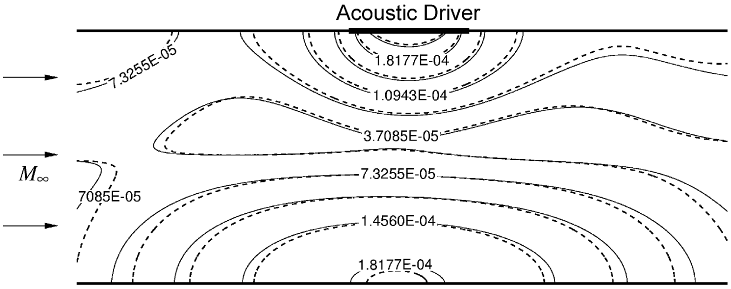

Fig. 8. Pressure amplitude contours inside the wind tunnel. Acoustic driver frequency = 625 Hz, $M_\infty = 0.15$. (——) numerical solution and (– – – –) analytical solution.

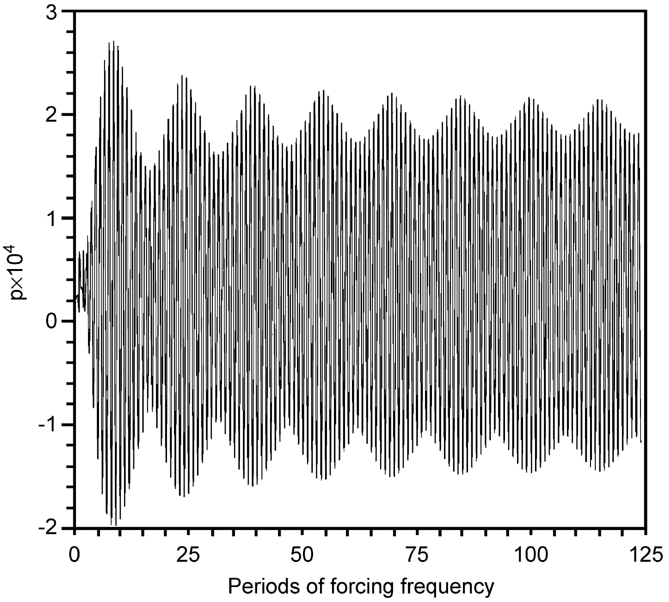

Fig. 9. Pressure time history measured on the bottom wall showing amplitude modulation.

But k_0 and ω_0 are also related by the dispersion relation Eq. (26). Substituting of Eq. (28) into Eq. (26), it is straightforward to find

$$\omega_0 = \frac{n\pi}{H}(1 - M^2)^{1/2}. \tag{29}$$

For the wind tunnel operating at Mach 0.15 the lowest frequency of the zero group velocity duct mode ($n = 1$) is 666.7 Hz.

Let us now examine the amplitude modulation phenomenon quantitatively. Suppose the pressure signal at a point comes from two sources with angular frequencies ω_1 and ω_2. Suppose the corresponding amplitudes are A and ε. It is assumed that the amplitude of the second signal is very small. Thus the pressure is given by

$$p(t) = Re\{A\,\mathrm{e}^{-\mathrm{i}\omega_1 t} + \varepsilon\,\mathrm{e}^{-\mathrm{i}(\omega_2 t+\phi)}\}, \tag{30}$$

where ϕ is an arbitrary phase. The envelope of the pressure time history is given by the absolute value of the expression in the curly brackets. Thus,

$$\begin{aligned}\text{Envelope of } p &= |A\,\mathrm{e}^{-\mathrm{i}\omega_1 t} + \varepsilon\,\mathrm{e}^{-\mathrm{i}(\omega_2 t+\phi)}| \\ &= A\left|1 + \left(\frac{\varepsilon}{A}\right)\mathrm{e}^{\mathrm{i}[(\omega_1-\omega_2)t-\phi]}\right| \\ &\cong A + \varepsilon\cos[(\omega_1 - \omega_2)t - \phi] + O(\varepsilon^2).\end{aligned} \tag{31}$$

Therefore, there is a small-amplitude modulation at a frequency f_{modulate} given by

$$f_{\text{modulate}} = \frac{1}{2\pi}(\omega_1 - \omega_2) \text{ or a period } T_{\text{modulate}} = \frac{2\pi}{\omega_1 - \omega_2} = \frac{1}{f_1 - f_2}. \tag{32}$$

For the problem under consideration, the forcing frequency is 625 Hz. The forcing period $T_{\text{forcing}} = 1.6 \times 10^{-3}$ s. The frequency of the zero group velocity duct mode is 666.7 Hz. By Eq. (32) the period of amplitude modulation is 2.40×10^{-2} s or $14.99T_{\text{forcing}}$. By measuring directly the period of amplitude modulation of the numerical simulation data (see Fig. 9), $T_{\text{modulation}}$ is found to be $14.93T_{\text{forcing}}$. This is very close to the exact value.

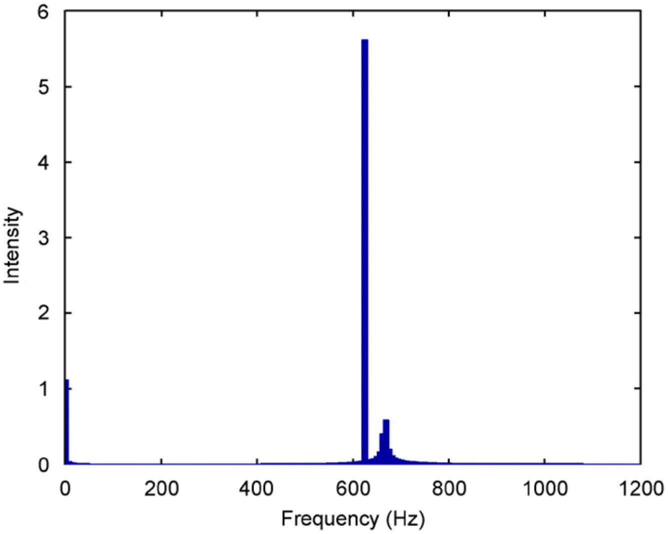

Fig. 10. Acoustic spectrum computed at a point 2.25″ downstream of the center of the acoustic driver on the bottom wall of the wind tunnel. The dominant spectral line is at 625 Hz. The secondary spectral line is at 665 Hz.

Since the pressure versus time results of the numerical simulation are available, it is possible to determine the pressure spectrum by direct calculation. In addition to the forcing frequency, the frequency of the zero group velocity duct mode should also be observed. Fig. 10 shows the computed noise spectrum at a point on the bottom wall of the wind tunnel 2.25 in (5.715 cm) downstream of the center of the acoustic driver. The dominant spectral line at 625 Hz is the forcing frequency. The much smaller spectral line is the frequency of the zero group velocity duct mode ($n = 1$). The measured value is 665 Hz, which is very close to the theoretical value of 666.7 Hz. It is worthwhile to point out that duct modes are formed by the coherent reflection of sound at the duct wall. In a numerical simulation, the frequency of the zero group velocity duct mode, therefore, depends critically on the quality of the computation scheme and numerical boundary conditions. That the numerically computed frequency is so close to the exact value verifies that the dispersion-relation-preserving marching scheme, the ghost point boundary condition (imposed at the walls) and the perfectly matched layer absorbing boundary condition (enforced at the two open ends of the computation domain) used in developing the computer code are accurate and of high quality.

3.3. Validation of wind tunnel computational code

Pressure measurements were carried out along the bottom wall of the wind tunnel in the companion experiment. In the experiment, the sound pressure level at the top was set at 130 dB. The wind tunnel speed was 30 m/s. The acoustic driver operated at 625 Hz frequency. Fig. 11 shows a comparison of the sound pressure level distribution along the bottom wall from the simulation results and from the experiment. Fig. 12 shows a corresponding comparison of the phase distribution. As can be seen, there is good agreement overall. It is to be noted that the sound pressure level differs by nearly 20 dB between the center of the wind tunnel and the farthest measurement point downstream. This is a fairly large dynamic range. It is, however, well captured by the numerical simulation providing further confidence in the accuracy of the computation code.

4. Numerical results and comparisons with experiments

Results obtained from numerical simulations are reported below. Comparisons between numerical results and experimental measurements are also presented.

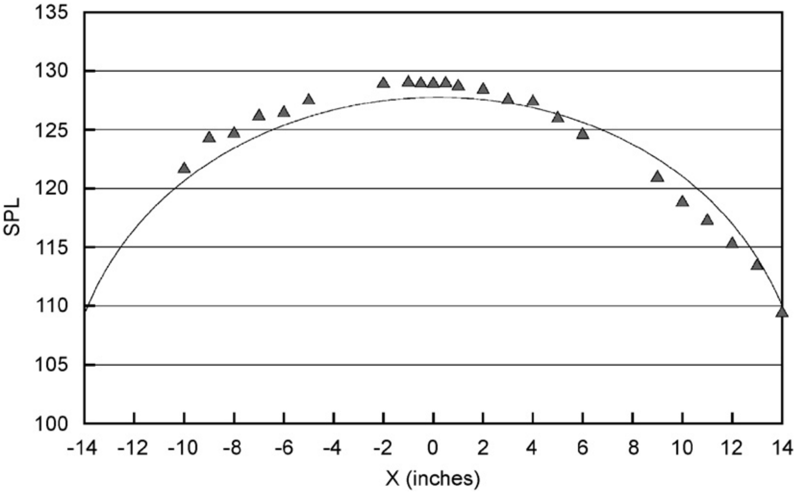

Fig. 11. Distribution of sound pressure level along the bottom wall of the wind tunnel. Speed = 30 m/s, frequency = 625 Hz: (——) numerical and (▲) experiment.

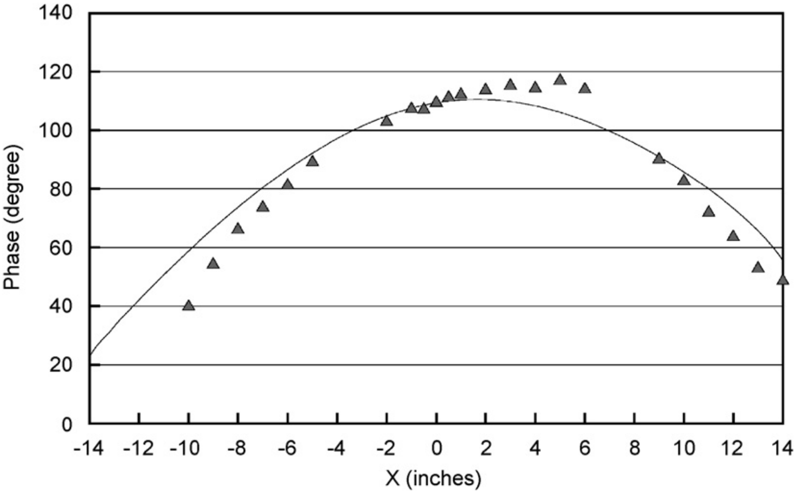

Fig. 12. Distribution of the phase of pressure signal along the bottom of the wind tunnel. Speed = 30 m/s, frequency = 625 Hz: (——) numerical and (▲) experiment.

4.1. Steady mean flow

The steady mean flow inside the slit resonator at a constant wind tunnel speed is found by time marching the numerical solution to a time-independent state (acoustic driver is turned off). Fig. 13a shows the computed streamline pattern at a wind tunnel speed of 30 m/s. Inside the resonator, the flow separates into two zones. At the mouth of the resonator, the flow field is made up of a vortex with clockwise rotation. This vortical flow is driven by the ambient flow from left to right. Deeper inside the resonator a counter-clockwise vortical flow is formed. This vortical flow is driven by the vortical flow at the mouth of the resonator. Fig. 13b shows an enlarged streamline pattern of the flow field at the mouth of the resonator. The separation streamline between the two vortical flows dips down inside the resonator. In addition to the general counter-clockwise circulation inside the resonator, there are two secondary flow regions at the upper corners of the resonator. The existence of these secondary circulation regions at the upper corners of the resonator is not expected *a priori*.

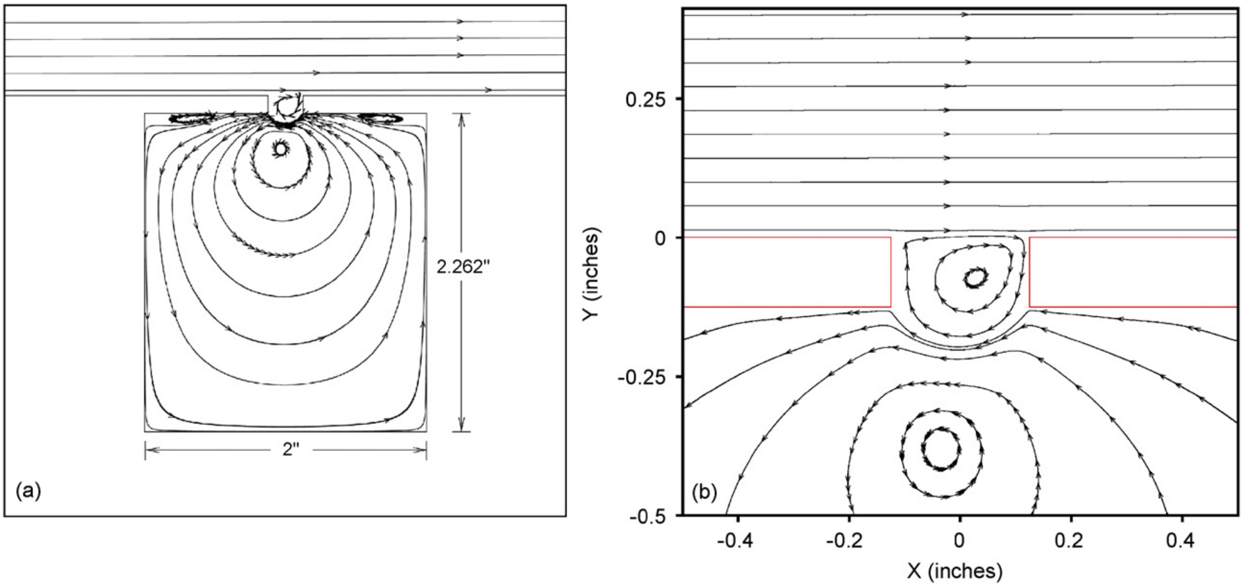

Fig. 13. (a) Streamlines of steady flow inside and outside the slit resonator. Wind tunnel speed = 30 m/s. (b) Enlarged streamline pattern at the mouth of the resonator.

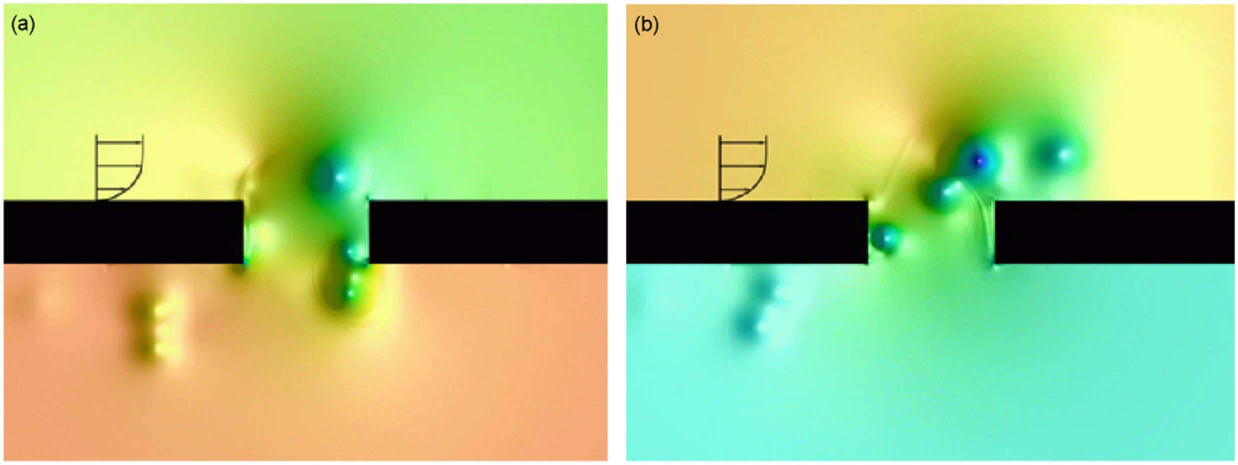

Fig. 14. Vortex shedding at the mouth of the resonator: (a) beginning of a cycle and (b) at a quarter of a period.

4.2. High-level incident sound waves

The flow field at the mouth of the resonator changes drastically as the incident sound pressure level increases. Above a certain sound pressure level the flow field is dominated by vortex shedding. Vortices are shed at the corners of the mouth of the resonator as fluid flows in and out in response to high and low pressure created by the incident sound. Figs. 14a and b are pictures of the density field of the flow. They show the vortices shed at two instants of a cycle of the incident wave. The incident wave sound pressure level is 140 dB. Fig. 15 shows the sequence of vortex shedding and subsequent merging. Fig. 15a is at the beginning of a cycle when pressure outside the resonator increases. Fluid starts the process of flowing into the resonator. The lone vortex A adjacent to the left wall is a trapped vortex. It was shed at the lower left corner of the mouth of the resonator at the end of the previous cycle when the fluid flowed out. The vortex was carried up by the flow, but

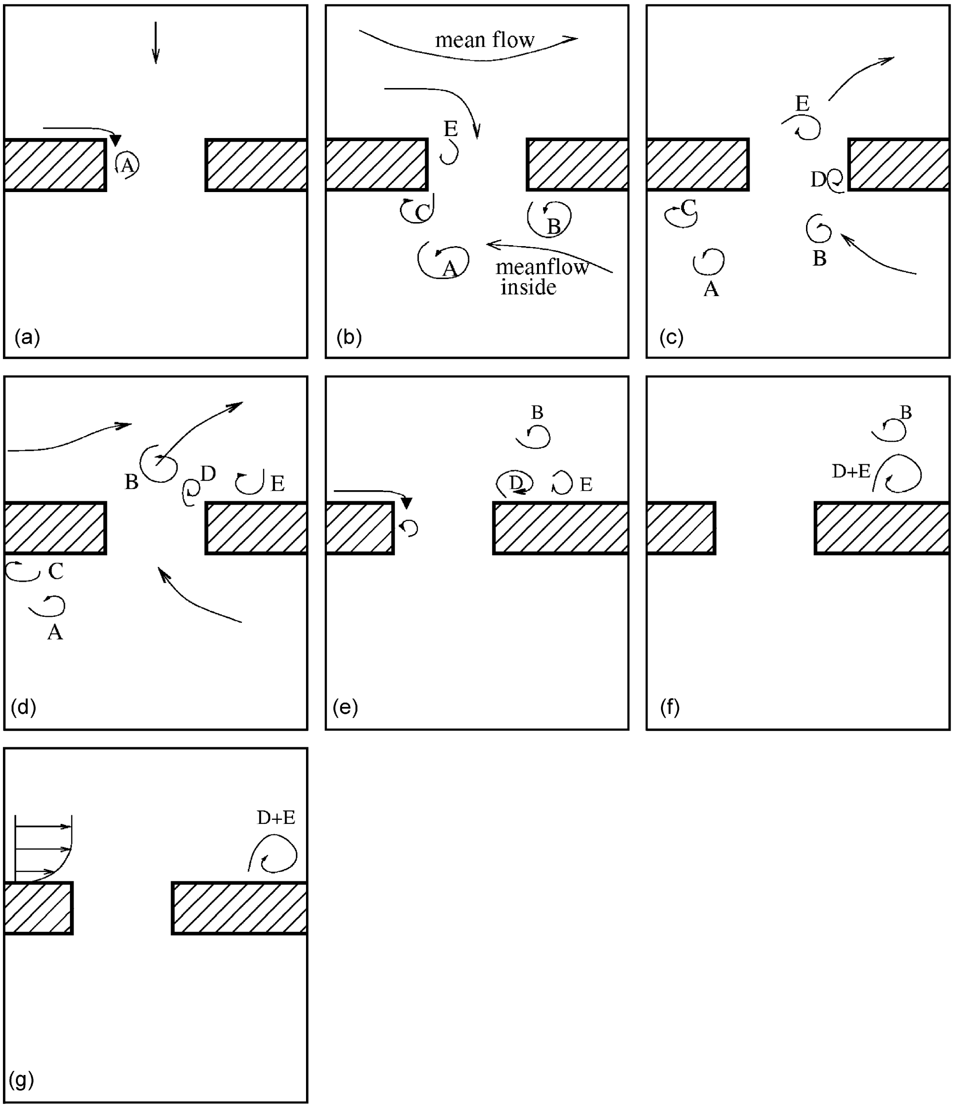

Fig. 15. Shedding and merging of vortices at the mouth of the resonator: (a) inflow begins; (b) strong inflow; (c) begin reverse flow; (d) strong outflow; (e) inflow begins again; (f) merging of vortices *D* and *E*; and (g) surviving vortex.

did not reach the outside to escape. The flow reversed direction and the vortex is swept downward. As the flow velocity into the resonator increases, three vortices *C*, *B* and *E* are shed at the three corners of the resonator opening. Vortices *C* and *E* have clockwise rotation. Vortex *B* has counter-clockwise rotation. This is shown in Fig. 15b. Because of the general counter-clockwise circulation inside the resonator, vortices *A* and *C* are convected to the left of the opening of the resonator and vortex *B* moves to the center. At this time, flow reversal takes place. The reversed flow creates vortex *D* with a clockwise rotation at the lower right corner as shown in Fig. 15c. The outflow ejects vortices *B*, *D* and *E* into the outside wind tunnel flow as indicated in Fig. 15d. These three vortices are then swept downstream to the right of the opening by the mean flow of the wind tunnel. This is shown in Fig. 15e. Vortices *D* and *E* have the same rotation. They merge into a large vortex. The two surviving vortices are shown in Fig. 15f. Vortex *B* has a counter-clockwise rotation. This is opposite to the natural rotation of the boundary layer fluid adjacent to the bottom wall of the wind tunnel. As a result, it becomes weaker and weaker. Finally, it disappears and is completely absorbed by the boundary layer flow. The remaining vortex $D+E$ is convected downstream. This vortex persists over a long distance

Fig. 16. Vortex downstream of the resonator.

downstream. In the simulation, it is observed even at a distance of 2–3 resonator widths downstream (see Fig. 16). This vortex may interfere with the flow of a downstream resonator if one is there.

4.3. Low-level incident sound waves

At low incident sound pressure level, e.g., 130 dB, there is no vortex shedding at the mouth of the resonator. The changing streamline patterns during a cycle as computed are shown in Fig. 17. Shown in this figure also are the streamline patterns measured experimentally by split film CT anemometry. Fig. 17a is at the beginning of a cycle. The flow in the opening of the resonator consists of a clockwise rotation. The outside flow simply slides over the resonator opening. Figs. 17b–h show the flow pattern at every 1/8 cycle later on. The experimental measurements are confined to the space outside the resonator. They do not show the streamline pattern inside the mouth of the resonator. By comparing the measured streamline patterns with the computed patterns, it is easy to see that there is good agreement over the entire cycle of oscillation. The good agreement is regarded as a validation of the present computer code.

4.4. Grid refinement

As a measure to ensure that proper resolution is used in the numerical simulation, a grid refinement test has been conducted. In this test, the spatial resolution of the code is increased by reducing the mesh size by a half. As a result, the time step is also reduced according to numerical stability requirement. Fig. 18 shows a comparison of the pressure time history measured at the center of the bottom of the cavity. Fig. 19 shows another comparison of the pressure time history at a point on the bottom wall of the wind tunnel at 2.25 in (5.72 cm) downstream of the center of the slit. There are only minor differences between the two computed results, indicating that there is sufficient resolution in the numerical simulation.

5. Summary and conclusions

A direct numerical simulation code based on the dispersion-relation-preserving scheme and advanced computational aeroacoustics numerical boundary treatments for simulating the flow and acoustic fields of a slit resonator in a grazing flow has been developed. The code has been verified by comparison with exact linear analytical solution. Direct numerical simulations of the grazing flow over a slit resonator with or without acoustic excitation have been carried out. Steady-state results show the existence of a vortex flow at the mouth

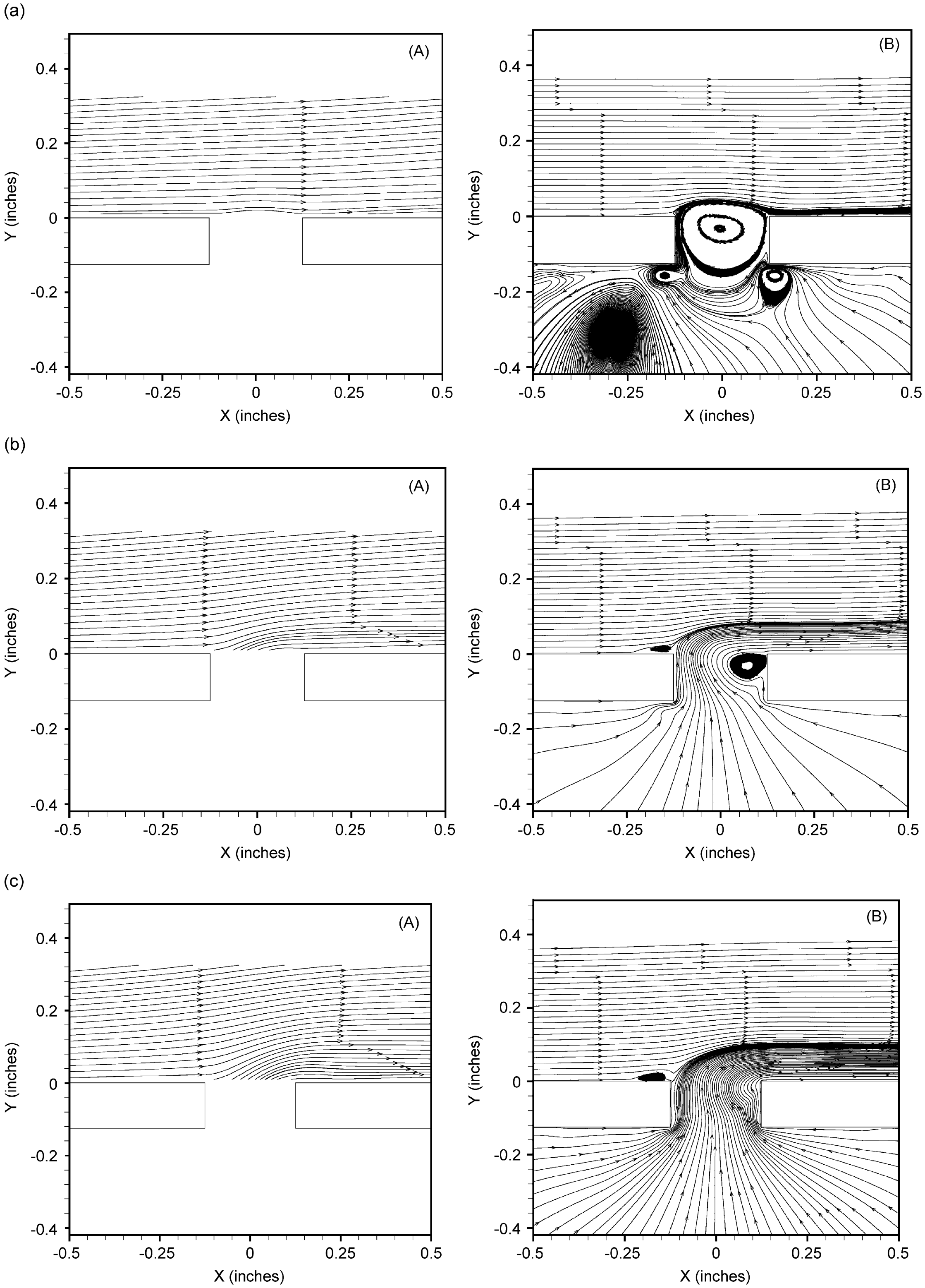

Fig. 17. Changing streamline pattern at low incident sound pressure level: (A) experiment and (B) simulation. T = period of oscillation. Wind tunnel speed = 30 m/s. Forcing frequency = 625 Hz: (a) t = beginning of a period; (b) $t = 0.125T$; (c) $t = 0.25T$; (d) $t = 0.375T$; (e) $t = 0.5T$; (f) $t = 0.625T$; (g) $t = 0.75T$; and (h) $t = 0.825T$.

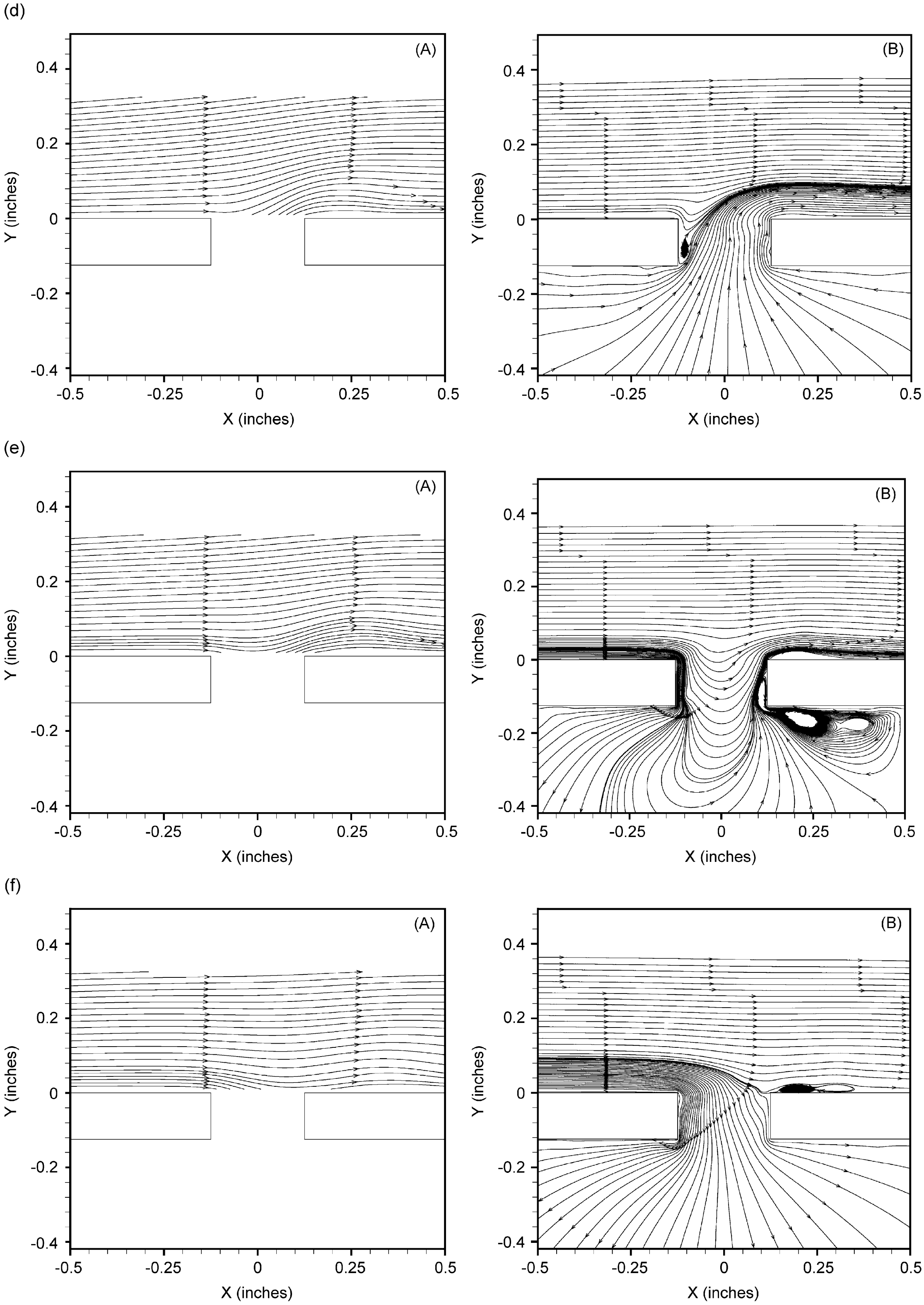

Fig. 17. (*Continued*)

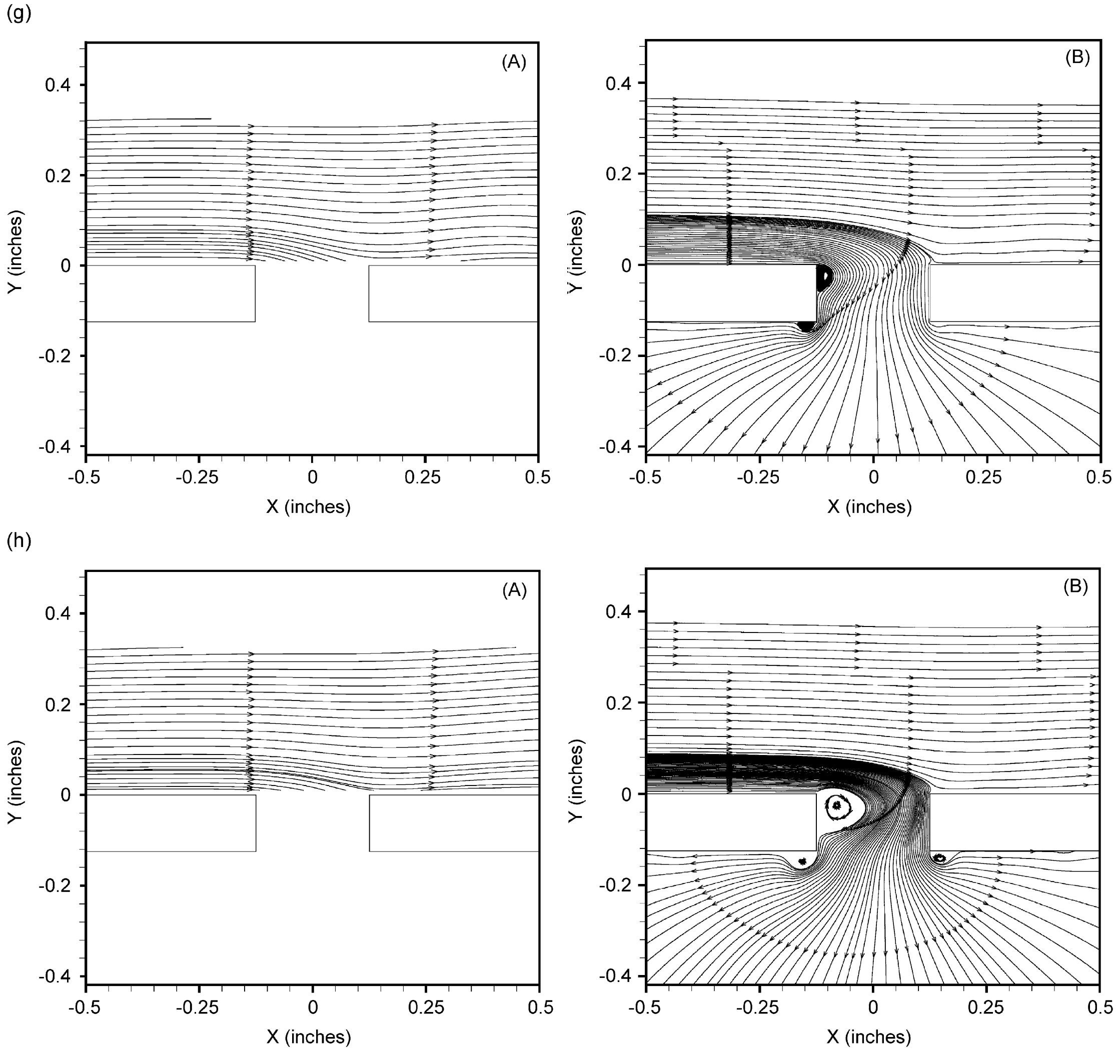

Fig. 17. (*Continued*)

of the resonator. Inside the resonator, the flow consists mainly of a counter rotating vortex. At high incident sound pressure level the flow at the mouth of the resonator is dominated by vortex shedding. Vortex shedding is the principal mechanism for the dissipation of acoustic energy. The vortex shedding and merging sequence is documented. Outside the resonator, a vortex with rotation compatible with the boundary layer flow persists for a long distance downstream. This vortex might interfere with the flow field of a downstream resonator. The present simulation is restricted to a single resonator, so that the process of interaction and its consequences cannot be evaluated at this time. This type of fluid mechanical interaction between neighboring resonators of an acoustic liner has not been included in all previous liner models. Future models should seriously consider taking this type of interaction into account. At low sound pressure level, there is no vortex shedding. The dominant acoustic damping mechanism is viscous dissipation in the oscillatory boundary layer around the mouth of the resonator. The streamline patterns found by numerical simulation agree well with experimental measurements.

The present computational model is not perfect and definitely has room for improvement. Firstly, the simulation is strictly speaking valid only for acoustic liners with large aspect ratio resonators. Secondly, the boundary layer in the present simulation is laminar. Recently, the authors have performed three-dimensional

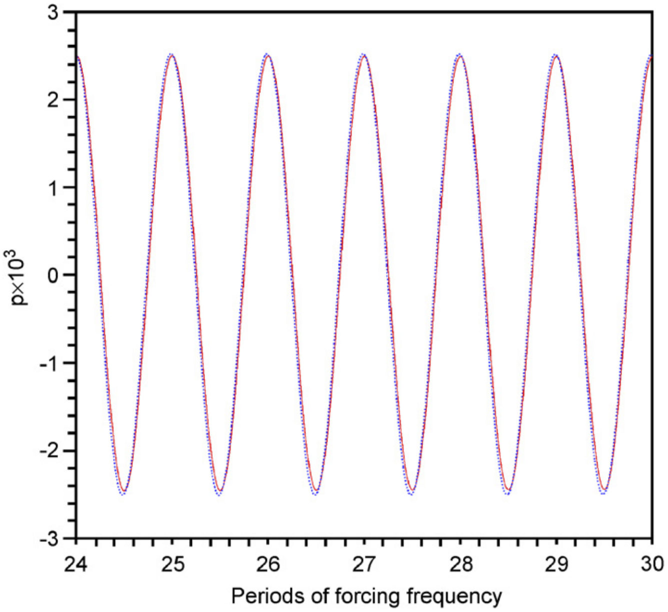

Fig. 18. Pressure time history measured at the center of the bottom wall of the cavity: (———) original grid; and (·········) refined grid at twice the resolution.

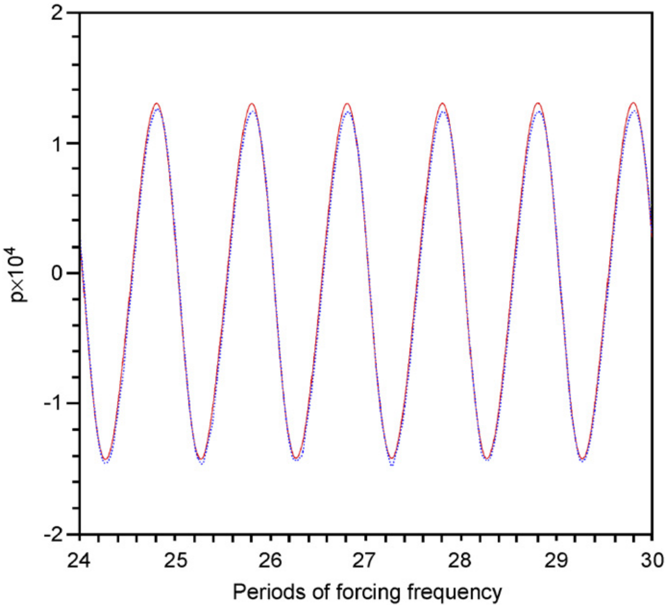

Fig. 19. Pressure time history at a point on the wind tunnel bottom wall at 2.25 in (5.72 cm) downstream of the center of the slit: (——) original grid; and (·········) refined grid at twice the resolution.

simulations of aspect ratios 1.25 and 2.5 resonators in a normal impedance tube. At high incident sound pressure level, vortex shedding was observed as in the case of a two-dimensional slit resonator. However, three-dimensional vortices form closed loops. It is not clear how far such vortices could persist in the presence of a turbulent grazing flow. The answers to these questions are obviously important to acoustic liner design. It is hoped that future work will address and clarify these issues.

Acknowledgments

This work was supported by NASA Contract NAS1-02108. The authors wish to thank Dr. Alan Hersh for his support of the project.

References

[1] U. Ingard, S. Labate, Acoustic circulation effects and the nonlinear impedance of orifices, *Journal of the Acoustical Society of America* 22 (1950) 211–219.

[2] U. Ingard, H. Ising, Acoustic nonlinearity of an orifice, *Journal of the Acoustical Society of America* 42 (1967) 6–17.

[3] T.H. Melling, The acoustic impedance of perforate at medium and high sound pressure levels, *Journal of Sound and Vibration* 29 (1993) 1–65.

[4] B.T. Zinn, A theoretical study of nonlinear damping by Helmholtz resonators, *Journal of Sound and Vibration* 13 (1970) 347–356.

[5] B. Phillips, Effects of high-wave amplitude and mean flow on a Helmholtz resonator, NASA Technical Memo TM X-1582, May 1969.

[6] T. Rogers, A.S. Hersh, The effect of grazing flow on the steady state resistance of square-edged orifices, *Proceedings of the Second AIAA Aeroacoustics Conference*, Langley, VA, USA, AIAA paper 75–493, 1975.

[7] A.L. Goldman, R.L. Panton, Measurement of the acoustic impedance of an orifice under a turbulent boundary layer, *Journal of Sound and Vibration* 60 (6) (1976) 1397–1404.

[8] J. Kompenhans, D. Ronneberger, The acoustic impedance of the orifices in the plate of a flow duct with a laminar or turbulent flow boundary layer, *Proceedings of the Sixth AIAA Aeroacoustics Conference*, Hartford, CT, USA, AIAA paper 80–0990, 1980.

[9] J.W. Kooi, S.L. Sarin, An experimental study of the Helmholtz resonator arrays under a turbulent boundary layer, *Proceedings of the Seventh AIAA Aeroacoustics Conference*, Palo Alto, CA, USA, AIAA paper 81–1988, 1981.

[10] B.E. Walker, A.F. Charwat, Correlation of the effects of grazing flow on the impedance of Helmholtz resonators, *Journal of the Acoustical Society of America* 72 (2) (1982) 550–555.

[11] A. Cummings, The effects of grazing turbulent pipe-flow on the impedance of an orifice, *Acustica* 61 (1986) 233–242.

[12] E.J. Rice, A model for the pressure excitation spectrum and acoustic impedance of sound absorbers in the presence of grazing flow, *Proceedings of the 1973 AIAA Aeroacoustics Conference*, Seattle, WA, USA, AIAA Paper 73–995, 1973.

[13] A.S. Hersh, B.E. Walker, J.W. Celano, Semi-empirical Helmholtz resonator impedance model, *Proceedings of the Seventh AIAA Aeroacoustics Conference*, AIAA paper 99–1825, 1999.

[14] I.D.J. Dupère, A.P. Dowling, The absorption of sound by Helmholtz resonators with and without flow, *Proceedings of the Eighth AIAA/CEAS Aeroacoustics Conference*, Breckenridge, CO, USA, AIAA Paper 2002–2590, June 2002.

[15] T. Elnady, H. Bodén, On semi-empirical liner impedance modeling with grazing flow, *Proceedings of the Ninth AIAA/CEAS Aeroacoustics Conference*, Hilton Head, SC, USA, AIAA Paper 2003–3304, May 2003.

[16] D. Ronneberger, The acoustic impedance of holes in the plate of flow ducts, *Journal of Sound and Vibration* 24 (1) (1972) 133–150.

[17] M.S. Howe, M.I. Scott, S.R. Sipcic, The influence of tangential mean flow on the Rayleigh conductivity of an aperture, *Proceedings of the Royal Society of London, Series A: Mathematics and Sciences* 452 (1996) 2303–2317.

[18] S. Kaji, M. Hiramoto, T. Okazaki, Acoustic characteristics of orifice holes exposed to grazing flow, *Bulletin of JSME* 27 (233) (1984) 2388–2396.

[19] S.M. Grace, M.S. Howe, K.P. Horan, The influence of grazing flow on the Rayleigh conductivity of an aperture of arbitrary shape, *Proceedings of the Third AIAA/CEAS Aeroacoustics Conference*, Atlanta, GA, USA, AIAA paper 97–1672, 1997.

[20] M.S. Howe, Influence of plate thickness on Rayleigh conductivity and flow-induced aperture tones, *Journal of Fluids and Structures* 11 (1997) 351–366.

[21] X. Jing, X. Sun, J. Wu, K. Meng, The effects of grazing flow on the acoustic behavior of orifices, *Proceedings of the Seventh AIAA/CEAS Aeroacoustics Conference*, Maastricht, Netherlands, AIAA paper 2001–2160, May 2001.

[22] P.A. Nelson, N.A. Halliwell, P.E. Doak, Fluid dynamics of a flow excited resonance, part I: Experiment, *Journal of Sound and Vibration* 78 (1) (1981) 15–38.

[23] W.J. Worraker, N.A. Halliwell, Jet engine liner impedance: an experimental investigation of cavity neck flow/acoustics in the presence of a Mach 0.5 tangential shear flow, *Journal of Sound and Vibration* 103 (4) (1985) 573–592.

[24] C. Malmary, S. Carbonne, Acoustic impedance measurement with grazing flow, *Proceedings of the Seventh AIAA/CEAS Aeroacoustics Conference*, Maastricht, Netherlands, AIAA Paper 2001–2193, May 2001.

[25] B.E. Walker, A.S. Hersh, Comparison of Dean's method and direct pressure/velocity measurement for slot resonator acoustic impedance determination, *Proceedings of the 10th AIAA/CEAS Aeroacoustics Conference*, Manchester, Great Britain, AIAA paper 2004–2839, May 2004.

[26] W.R. Watson, M.G. Jones, S.E. Tanner, T.L. Parrott, Validation of a numerical method for extracting liner impedance, *AIAA Journal* 34 (3) (1996) 548–554.

[27] W.R. Watson, M.G. Jones, T.L. Parrott, A quasi-3-D theory for impedance education in uniform grazing flow, *Proceedings of the 11th AIAA/CEAS Aeroacoustics Conference*, Monterey, AIAA paper 2005–2848, May 2005.

[28] T. Colonius, An overview of simulation, modeling and active control of flow/acoustic resonance in open cavities, *Proceedings of the Seventh AIAA/CEAS Aeroacoustics Conference*, Maastricht, Netherlands, AIAA Paper 2001–0076, May 2001.

[29] X. Gloerfelt, C. Bailly, D. Juve, Direct computation of the noise radiated by a subsonic cavity flow and application of integral methods, *Journal of Sound and Vibration* 266 (2003) 119–146.

[30] L. Larcheveque, O. Labbe, I. Mary, P. Sagaut, Large eddy simulation of subsonic flow over a deep open cavity, *Proceedings of the Third AFOSR International Conference on DNS and LES (TAICDL)*, Ruston, LA, 2001.

[31] K. Takeda, C.M. Shieh, Cavity tones by computational aeroacoustics, *International Journal of Computational Fluid Dynamics* 18 (2004) 439–454.

[32] C.K.W. Tam, P.J.W. Block, On the tones and pressure oscillations induced by flow over rectangular cavities, *Journal of Fluid Mechanics* 89 (1978) 373–399.

[33] J.E. Rossiter, Wind tunnel experiments on the flow over rectangular cavities at subsonic and transonic speeds, *Aeronautical Research Council Reports and Memoranda* no. 3438, 1964.

[34] C.K.W. Tam, K.A. Kurbatskii, Microfluid dynamics and acoustics of resonant liners, *AIAA Journal* 38 (8) (2000) 1331–1339.

[35] C.K.W. Tam, K.A. Kurbatskii, K.K. Ahuja, R.J. Gaeta Jr., A numerical and experimental investigation of the dissipation mechanisms of resonant acoustic liners, *Journal of Sound and Vibration* 245 (3) (2001) 545–557.

[36] C.K.W. Tam, H. Ju, M.G. Jones, W.R. Watson, T.L. Parrot, A computational and experimental study of slit resonators, *Journal of Sound and Vibration* 284 (2005) 947–984.

[37] C.K.W. Tam, K.A. Kurbatskii, Micro-fluid dynamics of a resonant liner in a grazing flow, *Proceedings of the Sixth AIAA/CEAS Aeroacoustics Conference*, Lahaina, Hawaii, AIAA paper 2000–1951, June 2000.

[38] F.M. White, *Viscous Fluid Flow*, second ed., McGraw-Hill, New York, 1991 (Chapter 3).

[39] C.K.W. Tam, J.C. Webb, Dispersion-relation-preserving finite difference schemes for computational acoustics, *Journal of Computational Physics* 107 (1993) 262–281.

[40] C.K.W. Tam, K.A. Kurbatskii, Multi-size-mesh multi-time-step dispersion-relation-preserving scheme for multiple-scales aeroacoustics problems, *International Journal of Computational Fluid Dynamics* 17 (2003) 119–132.

[41] F.Q. Hu, A stable perfectly matched layer for linearized Euler equations in unsplit physical variables, *Journal of Computational Physics* 173 (2001) 455–480.